Journal of GeoEngineering, Vol. 16, No. 2, pp. 047-059, June 2021
http://dx.doi.org/10.6310/jog.202106_16(2).1

AXIAL COMPONENT OF PLASTIC MODULUS OF SAND UNDER SLOW PERIODIC LOAD

Pingxin Xia [1], Chao Zeng [2], Longtan Shao [3*], Xiong Zhang [4], and Xiaoxia Guo [5]

ABSTRACT

Soil deformation under slow periodic load is of particular importance to predict the functionality of soil structure in a variety of engineering practices. However, lacking quantification on plastic deformation hinders the deformation analysis of soil subjected to slow periodic load. The axial component of plastic modulus is pivotal and is determined to calculate axial plastic strain and overall soil deformation. In this study, a static triaxial compression system was designed to perform a series of static cyclic triaxial tests and cyclic confined compression tests on a silica sand. The results showed that plastic strain increments decreased gradually, as the loading cycle proceeded, and finally only the elastic strain increment existed. The empirical equation of axial component of plastic modulus was formulated considering the effects of stress states, void ratios, and loading cycles. In combination with the description of elastic modulus, the axial strain increment in each loading cycle was formulated. In addition, in the unloading process of loading cycle, the volume contraction phenomenon was explained by unloading plastic strain and microscopic particle motion based on the present results.

Key words: Cyclic static triaxial test, cyclic confined compression test, axial component of plastic modulus, evolution of elastic modulus, sand, volume contraction.

1. INTRODUCTION

Slow periodic load — a rectangular wave load that ignores the loading rate and maintains a constant amplitude — is a ubiquitous phenomenon in many engineering practices, such as stacking and transportation of building materials, water impoundment and discharging on earth dams, cargo handling in container ports, and a tidal ebb and flow on coasts. It was of particular interest to investigate the deformation behavior of soil under slow periodic loads due to induced strength degradation and excessive settlement (Shin and Das 1999; Chiou *et al.* 2016; Dareeju *et al.* 2018; Zhao 2020). Thus, soil deformation analysis under slow periodic load was essential to precisely predict the functionality of soil structures. Generally, soil deformation induced by loading is composed of elastic and plastic deformations. To characterize the overall soil deformation, both elastic and plastic deformations should be precisely described (Hardin 1978). However, under slow periodic load, both elastic and plastic deformations occur concurrently at individual stress increments, which poses difficulty on the separate description of elastic and plastic deformations. This difficulty may be relieved by the introduction of elastic and plastic moduli which are assumed to be intrinsic properties of the soil. In terms of elastic and plastic moduli, they are defined to measure elastic and plastic strain increments corresponding to small stress increment $\Delta\sigma$, as schematically shown in Fig. 1. In this regard, the elastic strain increment $\Delta\varepsilon_e$ and plastic strain increment $\Delta\varepsilon_p$ can be separately described by the elastic modulus E_e and axial component of plastic modulus E_p on the premise that the elastic and plastic moduli can be accurately represented. Thus, both E_e and E_p play key roles in the accurate separation of elastic and plastic strains that are necessary to quantify the overall soil deformation.

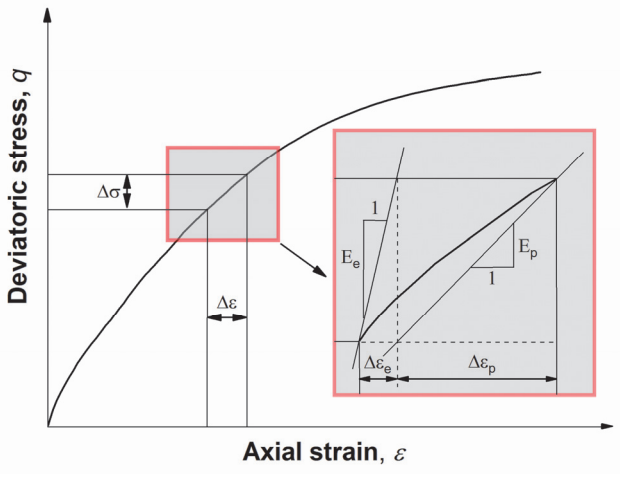

Fig. 1 Definitions of elastic modulus and axial component of plastic modulus

Manuscript received November 16, 2020; revised May 17, 2021; accepted May 17, 2021.

[1] Ph.D. Student, Dept. of Engineering Mechanics, Dalian University of Technology, Dalian 116024, China.
[2] Ph.D. Dept. of Civil, Architectural, and Environmental Engineering, Missouri University of Science and Technology, Rolla 65401, U.S.A.
[3*] Professor (corresponding author), Dept. of Engineering Mechanics, Dalian University of Technology, Dalian 116024, China (e-mail: shaolt@hotmail.com).
[4] Professor, Dept. of Civil, Architectural, and Environmental Engineering, Missouri University of Science and Technology, Rolla 65401, U.S.A.
[5] Associae Professor, Dept. of Engineering Mechanics, Dalian University of Technology, Dalian 116024, China.

It is widely accepted that the elastic modulus is clearly defined in the theory of elasticity, and its description is definite for a linearly elastic material. However, for soil, as a complicated elastoplastic media, the description of elastic modulus is vague in the stress-strain curve. In general, the prevalent representation of elastic modulus is obtained in the unloading process because the stress path inside the yield surface is assumed to produce only elastic strain (Anhdan and Koseki 2004; Kongsukprasert and Tatsuoka 2007; Taheri and Tatsuoka 2012; Taheri and Tatsuoka 2015). However, particulate materials yielded in the unloading process with a relatively large stress increment exceeding the transient elastic limit (Hardin and Blandford 1989; Hashiguchi 1989; Sawicki and Świdziński 1998), and consequently, the 'elastic' modulus in such a large-scale unloading process cannot represent the true elastic modulus. Regarding the accurate representation of elastic modulus, a previous study (Shao *et al.* 2018) provided a new description. It was obtained at the deformation steady state where the specimen response did not change dramatically when it was subjected to certain loading, and the stress-strain curve was a closed hysteretic loop. Elastic modulus obtained at deformation steady state was supported more favorably when compared to other representations (Shao *et al.* 2018). This description of elastic modulus was adopted in this study, and the deformation steady state was justified in the following analysis.

However, the representation of plastic modulus is unclear, so far, and formulations of plastic modulus were proposed based on various plasticity theories. By the best of our knowledge, the theories to define plastic modulus were multi-surface plasticity theories (Iwan 1967; Mróz 1967), two-surface plasticity theories (Dafalias and Popov 1975), boundary surface plasticity theories (Mroz *et al.* 1979; Dafalias and Herrmann 1986; Dafalias and Manzari 2004; Heidarzadeh and Oliaei 2018a), and generalized plasticity theories (Zienkiewicz and Mroz 1984; Weng 2013; Cen *et al.* 2018; Heidarzadeh and Oliaei 2018b). Among the plasticity theories, boundary surface plasticity and generalized plasticity are the two most common theories and can successfully characterize important soil behaviors, such as hysteresis, strain accumulation, dilatancy, and anisotropy (Ling and Liu 2003; Ling and Yang 2006; Heidarzadeh and Oliaei 2018a). However, both boundary surface plasticity and generalized plasticity are still unsatisfactory in describing soil's plastic deformation due to the unclear and complicated definition of plastic modulus. For example, in boundary surface plasticity, the plastic modulus is regarded as a parameter of yield surface and depends on the size, position, and shape of the yield surface. In addition, its evolution is assumed and simplified in advance. For generalized plasticity, it does not explicitly define the yield and plastic potential surfaces, but it specifies loading and unloading plastic moduli as appropriate functions of stress vectors and state parameters. With pre-posterior assumption and simplification, the plastic modulus from boundary surface plasticity and generalized plasticity most likely deviate from the true value. Overall, although the development of plasticity theories is important to predict plastic deformation by hardening law and flow rule, as an alternative, it is more practical to define a plastic modulus with a clear physical meaning.

It was also noted that the plastic modulus is often expressed as being related to the stress vector, but the coupled stresses cannot reflect the evolution of the plastic modulus in a certain stress direction. There is an axial component of the plastic modulus that controls the magnitude of plastic strain increment in that direction. To present the evolution of axial component of plastic modulus with axial stress, the axial component of the plastic modulus can be decoupled. According to the geometric relation in Fig. 1, when the elastic modulus and the tangent modulus for the total strain increment are known, the axial component of plastic modulus can be directly decoupled and associated axial plastic strain increment can also be determined. In this way, the evolution of plastic modulus in axial stress direction can be presented.

This study was intended to develop an empirical formulation for the axial component of plastic modulus and to predict the axial plastic strain increment under slow periodic load. In combination with the description of elastic modulus from a previous study (Shao *et al.* 2018), the elastic strain and plastic strain increments can be separately described and the overall deformation formulated under slow periodic load. The structure of this study was briefly introduced as follows. First, cyclic triaxial test with slow periodic load (CSTT) using an advanced digital image measurement system (DIMS) and cyclic confined compression test (CCCT), were conducted on the silica sand. The deformation steady state was reached when the loading cycle was large enough. The elastic modulus was obtained at the deformation steady state and the axial component of plastic modulus was then calculated. Then, the evolution of moduli during slow periodic load was presented, especially the axial component of plastic modulus, and the dependency of axial component of plastic modulus on stress state and void ratio was formulated. An empirical model for the axial component of plastic modulus under a slow periodic load was proposed for sand. In the discussion section, the deformation steady state — where previous results lay on — is justified by the concept of deformation modulus growth rate. Finally, the volume contraction phenomenon in the unloading process was explained by the unloading plastic strain and microstructure change of specimen.

2. EXPERIMENTAL PROCEDURE

2.1 Experimental Technique

In this study, a triaxial compression test system was designed to perform CSTT. The triaxial compression test system consisted of a static triaxial test system and a DIMS (see Fig. 2(a)). In the static triaxial test system, the servo control system applied static loads to the mounted specimen. The servo control system was mainly composed of two actuators (two piston cylinders). Cylinder 1 was controlled by a servo motor to provide constant pressure, and Cylinder 2 converted the constant pressure into constant axial loads on the specimen. There are two merits of this newly designed servo control system. Initially, two actuators converted pressure into the load to avoid servo motor vibration and misalignment, which is a common issue for the single axial actuator. Secondly, two actuators applied smooth loads, especially for small strain slow periodic load tests. Then, the applied load by the servo control system was measured by the internal load cell submerged in the pressure cell. This measurement by submerged load cell avoided extraneous friction between loading rod and pressure cell. This new design produced more accurate results than conventional measurements. For the radial loading, another pressure controller was employed to maintain constant confining pressure, as shown in Fig. 2(a).

In DIMS, the system was composed of a new pressure cell, a complementary metal-oxide-semiconductor camera, and a camera bracket. This measurement method discretized the specimen into several four-node finite elements by printing grids on

the rubber membrane and taking corners of the grids as the nodes of the finite elements. Tracking the deformation of the finite elements by edge detection and corner detection. Then, the deformation of the whole specimen surface was captured by the two flat mirrors that were positioned at a 120° angle behind the specimen. Finally, the deformation of the whole surface was obtained by conducting splicing and error correction on the images of the front and back faces in the mirrors.

The specimen was a cylinder 80 mm in height and 39.1 mm in diameter in CSTT, and it was wrapped in a black rubber membrane, on which white squares (7 mm by 7 mm) were printed. In this manner, the whole surface of the specimen meshed, and the corners of the white-black grid on the images were recognized using a subpixel corner-detector algorithm (Fig. 2(b)), and then, the coordinates of the corners on the entire surface of the specimen were obtained. The recorded data for the entire circumference of the specimen were divided into three parts: the images of the front face and the two side parts of the back faces in the mirrors; the data of the two side parts had to be mirrored (see Fig. 2(c)). Then, the recorded data were processed in three steps to obtain the strains on the entire surface of the specimen. First, the curved cylindrical surface images were spread onto the *x*-*y* plane using normalized pixel equivalents with respect to the differences in the distances between the corners and the lens, because the images were plane projections of the specimen. Second, to obtain a view of all corners on the entire surface, the images of the front and back faces in the mirrors were spliced together using the overlapping corners in the images. Third, the strains of each element on the whole surface were calculated by the shape function of the four-node iso-parametric element and the corresponding geometric transformation matrix with the image-tracked displacements of the corners. There were 16 rows of corner points on the black rubber membrane. Considering the effect of the bedding error on the test results, only the central 12 rows (excluding 4 rows close to the sample pedestal and

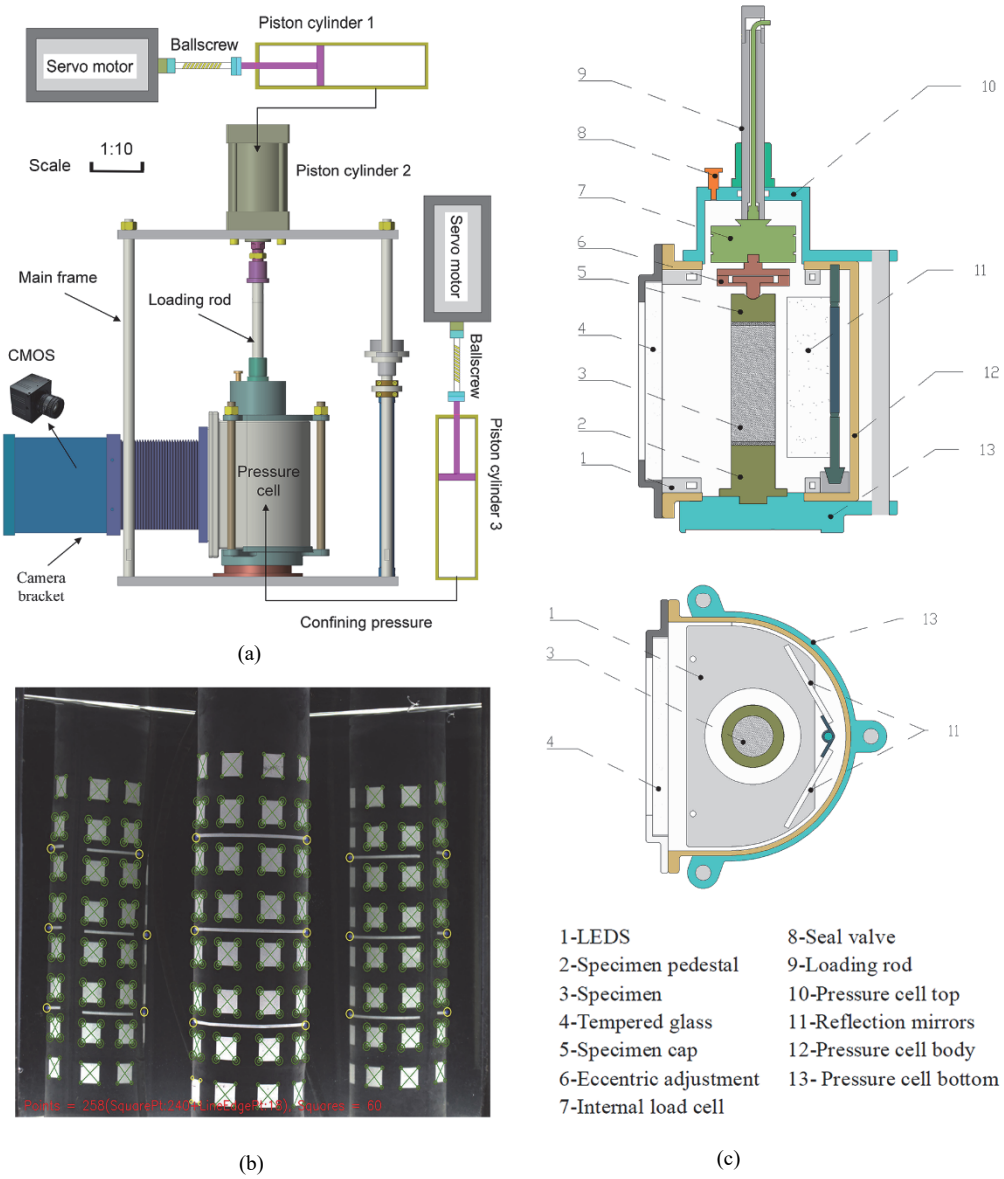

Fig. 2 Triaxial compression test systems: (a) components of test apparatus in CSTT; (b) image of corner detected and tracked; and (c) longitudinal and cross-sectional views of image pressure cell

the sample cap) were selected to calculate the overall average axial strain. The 4 rows near the two ends of the specimen were discarded because it would have caused bedding errors. This consideration obtained more accurate and uniform axial deformation. Another advantage of DIMS was that non-contact measurement avoided disturbing the specimen compared to the local gauges (including LVDT and LDT, Local Deformation Transducer). Furthermore, the accuracy of the axial and radial strain measurements was detected by high-precision strain gauges with strain accuracy of 10^{-7} that were evenly distributed on the hollow aluminum cylinder (printed with the same size grid); the calibration system is shown in Fig. 3. The calibration system was composed of a strain tester, control software, a pressure cell, and strain gauges. The results measured by the strain gauges were assumed to be the "true values" due to the high strain measurement accuracy of 10^{-7}; whereas, the results from the DIMS were the "test values"; the measurement precision of the DIMS was estimated by comparing the difference between the "true values" and the "test values". In all calibration tests, the calibration results were discrete due to calibration errors. The calibration results fell on various accuracy thresholds corresponding to different accuracy assurance rates. Table 1 shows that the measurement errors corresponded to the assurance rates of 75% and 95%, respectively. Although accuracy under the 95% assurance rate decreased compared to the 75% assurance rate, the strain accuracy of DIMS is still acceptable. Finally, the measurement accuracy of DIMS was in the order of $10^{-4} \sim 10^{-5}$. Further details regarding the accuracy calibration on this optical method were provided in previous studies (Liu 2012; Shao *et al.* 2016; Shao *et al.* 2012).

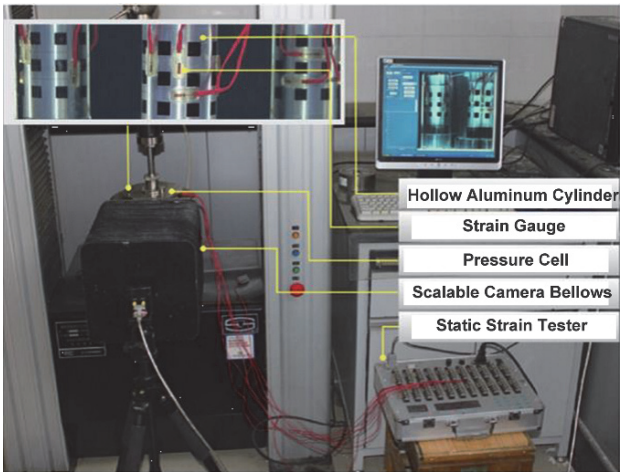

Fig. 3 Strain accuracy analysis system for DIMS

Table 1 Accuracy verification

Assurance rate	Front surface error, %		Mirror surface error, %	
	Axial	Radial	Axial	Radial
95%	0.0039	0.0017	0.015	0.011
75%	0.002	0.0009	0.0045	0.004

Note: In the accuracy calibration test of the measurement method, the measurement accuracy value always fluctuated. The ratio of the number of occurrences of a certain measurement accuracy value to the total number of tests is called the assurance rate.

An oedometric test apparatus was employed to carry out CCCT by applying repeated loadings. A constant load was maintained by applying weights. The specimen was 20 mm in height and 61.8 mm in diameter, and the deformation of the specimen was recorded by a dial indicator.

2.2 Test Materials and Test Plan

The test material was the silica sand. The grain size distribution curve is shown in Fig. 4, and the minimum and maximum densities were 1.21 and 1.67 g/cm^3, respectively. The specific gravity, uniformity coefficient, and curvature coefficient were: G_s = 2.678, C_u = 2.53, and C_c = 0.85, respectively. The relative density of each specimen is listed in Table 2. All silica sands for testing was oven-dried at 100°C for 24 hours and left at ambient temperature for several hours to reach temperature equilibrium. The specimens were directly prepared in a dry state in four layers on the sample pedestal. To achieve a uniform specimen, the lower layers were prepared in a slightly looser state compared with the middle and upper layers. In CSTT, each specimen was tested under dry conditions by applying a single axial load, and the confining pressure was kept constant during the cycle, as shown in Fig. 5(a).

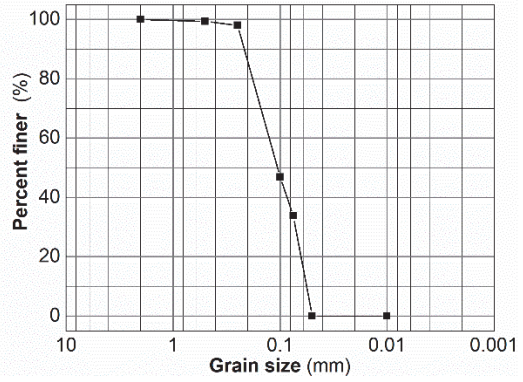

Fig. 4 Grain size distribution curve of the test material

Table 2 Test plan

Test number	Initial dry density ρ_d (g/cm^3)	Initial void ratio	Initial relative density	Confining pressure σ_3 (kPa)	Static-stress amplitude q_{max} (kPa)	Cycle number N
CSTT11	1.45	0.847	0.60	200	400	110
CSTT21	1.50	0.785	0.70	200	400	110
CSTT31	1.55	0.728	0.80	200	400	110
CSTT41	1.60	0.674	0.88	200	400	110
CSTT51	1.65	0.623	0.97	200	400	110
CSTT22	1.50	0.785	0.70	100	400	110
CSTT23	1.50	0.785	0.70	150	400	110
CSTT24	1.50	0.785	0.70	250	400	110
CSTT25	1.50	0.785	0.70	300	400	110
CCCT01	1.45	0.847	0.60	–	0 → 50 → 100 → 200 → 300 → 200 → 100 → 50 → 0	32
CCCT02	1.50	0.785	0.70	–		32
CCCT03	1.55	0.728	0.80	–		32

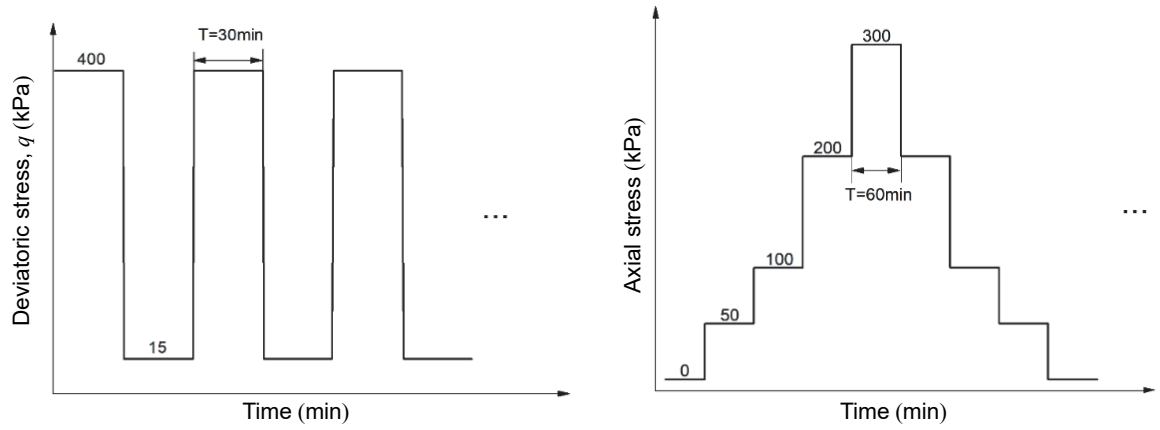

(a) CSTT (b) CCCT

Fig. 5 Stress time histories

The minimum and maximum deviatoric stresses were 15 kPa and 400 kPa, respectively, and both were sustained for 30 minutes. In CCCT, cyclic axial stepwise loading had five different levels of stress, and each level of stress was sustained for 60 minutes in reloading and unloading, as shown in Fig. 5(b). Note that loading duration in CCCT was different from that in CSTT to ensure sufficient strain accumulation of the specimen. Before continuing to the next stage or cycle, the specimens were assumed to have completed the deformation of the current loading step. The test plan included various test conditions to consider the effects of the initial void ratio and confining pressure. Table 2 lists the test plan.

3. RESULTS

3.1 Deformation Steady State in Cyclic Loading

To describe the results concisely, the representative test results were taken as examples to discuss the deformation steady state of the silica sand under slow periodic load. Figure 6 shows the typical strain-time relation, and the inset in the graph shows the local enlargement region. Hereafter, unless stated, the strain mentioned in this study referred to axial strain. The results illustrated that the strain gradually accumulated. The rate of strain accumulation progressively reduces as the loading cycle proceeds, and the magnitude of strain asymptotically became constant as loading approached the ultimate state. This trend is more obvious for specimen with high confining pressures (Fig. 6(a)) or large initial void ratios (Fig. 6(b)). In this study, the ultimate state where no strain accumulated was regarded as the deformation steady state. The ideal deformation steady state is difficult to obtain, when the strain increment of two adjacent cycles is lower than the lower limit of measurement accuracy, *i.e.,* 10^{-4}, it was assumed the specimen reached the deformation steady state. Note that the deformation characteristics of the specimen in the steady state did not change significantly, and the shape of the stress-strain curve remained unchanged. This steady state was reached at the given loading/unloading stress amplitude, and the particles in the corresponding specimen were in equilibrium, meaning, the particles reciprocate during a loading/unloading stress cycle. In fact, the deformation steady state was a quasi-elastic state in terms of the almost closed stress-strain curve. If the applied stress exceeds the loading/unloading stress amplitude, the current balance would be broken, resulting in a new plastic deformation. Conversely, one must note that the concept of deformation steady state in this paper was different from the traditional critical state, which was the concept introduced by Roscoe in the Cam-Clay model for monotonic loading, but the steady state or shakedown in cyclic loading. The steady state refers to a gradual state reached by the specimen under cyclic loading with constant stress amplitude, which reflected the final state of the strain hardening process. The critical state is usually used to describe the limit state after a monotonic shear failure. Critical states were avoided because they could have caused misunderstandings of specimens' shear states. All test conditions were far away from the critical state. The deformation steady state indicated the dominance of elastic deformation and the negligibility of plastic deformation, which was justified in the discussion section. For more details of deformation steady state, refer to studies (Anhdan and Koseki 2004) and (Zeng and Shao 2016).

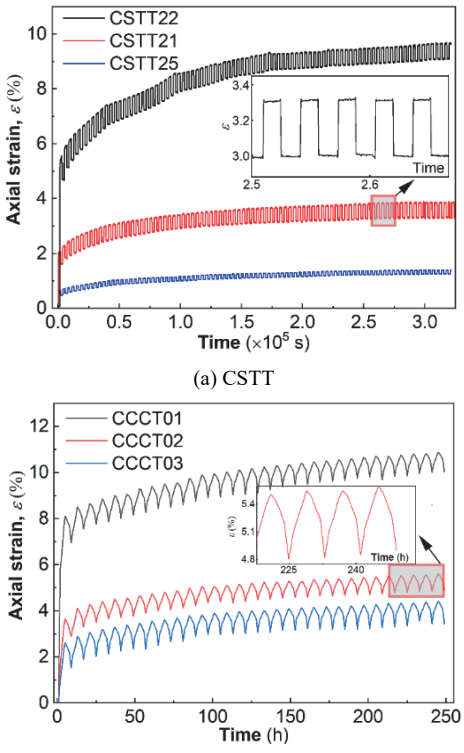

(a) CSTT

(b) CCCT

Fig. 6 Curves of axial strain versus time

3.2 Moduli Relationship in Cyclic Loading

The incremental deformation at each stress increment had elastic and plastic components. The elastic strain increment $\Delta\varepsilon_e$ and plastic strain increment $\Delta\varepsilon_p$ can be separately described by the elastic modulus E_e and axial component of plastic modulus E_p on the premise that the elastic and plastic moduli can be accurately represented (see Fig. 1). The relation of elastic and plastic strain increments can be expressed as:

$$\Delta\varepsilon = \Delta\varepsilon_e + \Delta\varepsilon_p \tag{1}$$

where $\Delta\varepsilon$ is the axial strain increment. Without being stated, the subscripts e and p denote elastic and plastic in the following analysis. Based on geometric relation in Fig. 1, the moduli are expressed as:

$$E = \frac{\Delta\sigma_1}{\Delta\varepsilon} \tag{2a}$$

$$E_e = \frac{\Delta\sigma_1}{\Delta\varepsilon_e} \tag{2b}$$

$$E_p = \frac{\Delta\sigma_1}{\Delta\varepsilon_p} \tag{2c}$$

$$\frac{1}{E} = \frac{1}{E_e} + \frac{1}{E_p} \tag{2d}$$

where E and $\Delta\sigma_1$ are the deformation modulus and axial stress increment, respectively. Equation (2d) was derived from Eqs. (1), (2a), (2b), and (2c). The elastic modulus was calculated in deformation steady state, and it was assumed that elastic modulus remained constant responding to different cycles (This assumption will be verified in the discussion section). Related studies about the constant elastic properties were reported. For example, Pradhan *et al.* (1989) separated the plastic shear strain by assuming that the elastic shear strain was constant under cyclic loading. Karg and Haegeman (2009) stated that the elastic properties of the soil at a small strain level remained constant during cyclic loading. This statement was validated when the stress-strain hysteresis loop steadied, that is, at the deformation steady state. Thus, in this study, the modulus in deformation steady state was regarded as the elastic modulus at all loading cycles. Consequently, for each cycle, with measured $\Delta\varepsilon$ in each $\Delta\sigma_1$ increment, the axial component of plastic modulus E_p can be directly decoupled from calculated deformation modulus E, and its evolution with respect to cyclic loading was acquired as well, which eased the description of the strain accumulation under cyclic loading. Noted that the elastic strain increment was the accumulation of proceeding elastic strains at different stress levels (accompanied by plastic strain), which is called the hypo-(quasi)-elastic model (Tatsuoka and Kohata 1994; Hoque and Tatsuoka 1998; Di Benedetto *et al.* 2002; Hongnam and Koseki 2019), meaning that in large plastic deformation, the elastic strain increment was isolated and exceeded amplitude of 0.001% which is typically the limit for evaluating elastic modulus. For example, the magnitude of elastic strain increment of CSTT21 in deformation steady state was greater than 0.2%. Correspondingly, the elastic modulus obtained in this study was an average elastic modulus for the given axial stress increment. This is different from the elastic probe tests in which a single or multiple unreload cycle(s) had small amplitudes of cyclic strain with the order of 10^{-5}, and they were applied at different stress points to evaluate the elastic modulus (Shibuya *et al.* 1992; Hicher 1996; Hoque and Tatsuoka 2004; Taheri and Tatsuoka 2015).

Under slow periodic load, moduli E and E_p vary with loading cycles. That is, the moduli relation in Eq. (2d) incorporated the effect of loading cycles. To see the dominance of E_e and E_p with loading cycles, the moduli evolution was analyzed. In CSTT, the lines in Fig. 7(a) represent these moduli. The deformation modulus E is represented by a straight line between the reloading starting point and unloading starting point in the individual loading-unloading cycle, as shown in the inset graph. In particular, the deformation modulus E in the deformation steady state was the elastic modulus E_e. The axial component of plastic modulus E_p is decoupled according to Eq. 2(d). Note that E_e was calculated in the deformation steady state and kept constant at different loading cycles. In this way, the moduli evolution was intuitively reflected by the inclination of the lines. Different in CCCT, each loading-unloading cycle had four stress increments as shown in Fig. 5(b), indicating that deformation modulus E has four representative lines corresponding to different stress levels, as shown in Fig. 7(b). In Fig. 7(b), the definition of moduli (E, E_e and

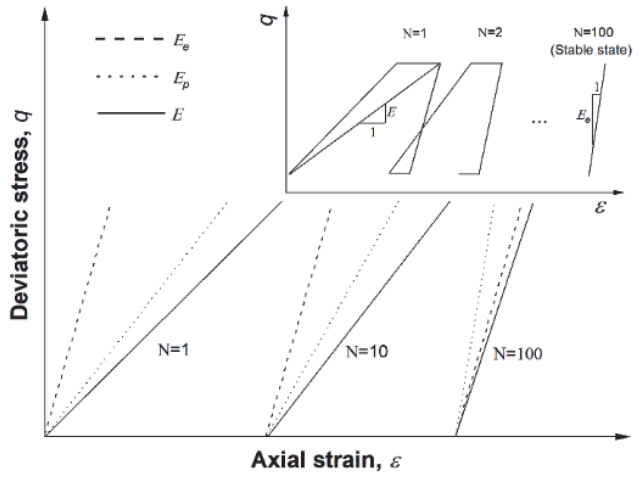

(a) CSTT

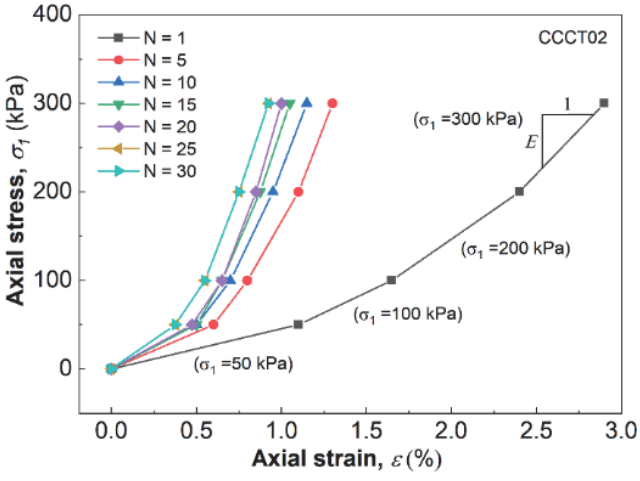

(b) CCCT

Fig. 7 Stress-strain curves under different cycles

E_p) in CCCT is different from that in CSTT because of the variable confining pressure ($d\sigma_3 \neq 0$) in CCCT. However, here, the dependence of moduli on stresses, including axial stress and confining pressure, is regarded as a superimposed effect. The moduli calculated directly from the experimental results included the combined effect of axial stresses and confining pressures.

The deformation modulus was determined by a lower quantity between elastic modulus and plastic modulus, as seen from Eq. (2d). This was validated from experimental data. In CSTT, the deformation modulus depended on the axial component of plastic modulus in the initial cycles because the axial component of plastic modulus was the smaller one compared to the elastic modulus. As the axial component of plastic modulus gradually exceeded the elastic modulus, the deformation modulus weighted toward the elastic modulus and asymptotically approached the elastic modulus. In CCCT, the same trend of curves is observed in Fig. 7(b). It was clear that the representative lines shifted to the left and progressively approached the deformation steady state with the increased cycle number, indicating that the deformation modulus continuously approached the elastic modulus but did not exceed it.

3.3 Axial Component of Plastic Modulus

The hardening behavior of the specimen in cyclic loading caused the continuous evolution of the axial component of plastic modulus, which was different from the evolution of the elastic modulus. A previous study (Zhao and Zhang 2014) showed that the axial component of plastic modulus increased with loading cycles and was finally constant. Detailed introduction on plastic modulus in cyclic loading referred to literature (Das 2014). In this study, the axial component of plastic modulus was considered a function of stress state (namely, σ_1 and σ_3), void ratio, and the number of cycles. Due to the constant axial stress increment and confining pressure in CSTT, the evolution of axial component of plastic modulus was more easily captured. The axial component of plastic modulus versus loading cycles in CSTT is shown in Fig. 8. The evolution of axial component of plastic modulus can be fitted by the following exponential form:

$$E_p = \gamma_1(\sigma_1, \sigma_3, e) \cdot \exp(\eta \cdot N) \tag{3}$$

where $\gamma_1(\sigma_1, \sigma_3, e)$ is a state parameter as a function of confining pressure σ_3, axial stress σ_1, and void ratio e, and η and N are constant and the number of cycles, respectively. It should be noted that for better illustration, only experimental data with $N \leq 70$ are presented in Fig. 8. With $N > 70$, plastic strain increment becomes smaller at each stress increment and leads to the energetic increase of the curve.

To find the explicit form of $\gamma_1(\sigma_1, \sigma_3, e)$ in Eq. (3), the effects of stress state and void ratio on the axial component of plastic modulus were analyzed separately with constant loading cycle (N = 1). The stress state dependence of axial component of plastic modulus was different from that of elastic modulus. The axial component of plastic modulus decreased with increasing axial stress, and it increased with increasing confining pressure (Weng 2013). Figure 9(a) depicts the relationship between the axial component of plastic modulus and the normalized confining pressure, which can be expressed by:

$$E_p = G \cdot p_a \cdot \left(\frac{\sigma_3}{p_a}\right)^m \tag{4}$$

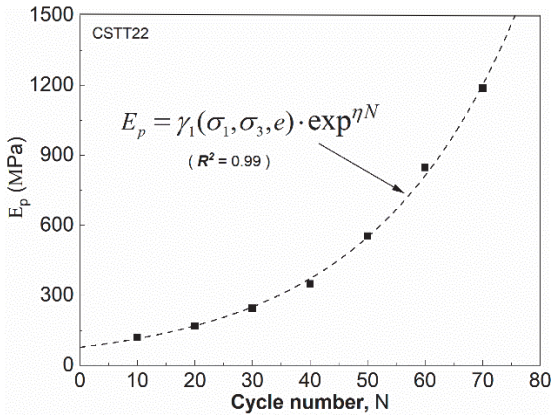

Fig. 8 Axial component of plastic modulus versus the number of cycles

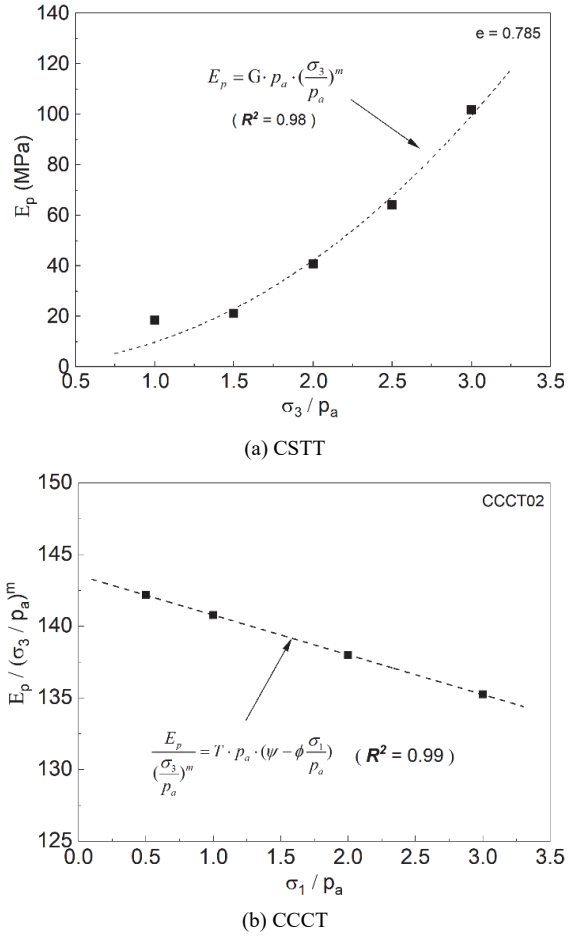

Fig. 9 Dependency of axial component of plastic modulus on (a) confining pressure (CSTT) and (b) axial stress (CCCT)

where G and m are the constants, and p_a is the atmospheric pressure. The stress state dependency of the axial component of plastic modulus did not show the representation of σ_1 in Eq. (4) because of the constant axial stress increment in CSTT. In Eq. (4), σ_1 is a value and incorporated in G. The dependence of axial component of plastic modulus on σ_1 can be obtained from CCCT, where σ_1 and σ_3 proportionally increase in the loading scheme. To present the axial stress dependency of axial component of plastic modulus, the axial component of plastic modulus is initially normalized by

Eq. (4). From experimental data, the dependency of axial component of plastic modulus on axial stress is shown in Fig. 9(b). It was seen that axial component of plastic modulus decreased linearly with axial stress. Thus, the stress state dependency of axial component of plastic modulus can be expressed by the following empirical formulation:

$$E_p = T \cdot p_a \cdot \left(\psi - \phi \frac{\sigma_1}{p_a} \right) \cdot \left(\frac{\sigma_3}{p_a} \right)^m \tag{5}$$

where T, ψ, and ϕ are the constants.

Several empirical formulas for void ratio were proposed to describe the response of soils in cyclic loading (Hardin and Richart 1963; Hardin and Drnevich 1972; Kohata *et al.* 1997; Wichtmann *et al.* 2005; Heidarzadeh and Oliaei 2018a). In this study, a modified void ratio function, originally proposed by Hardin and Richart (1963), was used to fit experimental data. The dependency of the axial component of plastic modulus on the void ratio is plotted in Fig. 10, which can also be expressed by modified Hardin's (Hardin and Richart 1963) model:

$$E_p = H \cdot p_a \cdot f(e) \tag{6}$$

where H is the constant, and $f(e) = (2.17 - \chi \cdot e)^2/(1 + e)$ is the void ratio function originally proposed by Hardin and Richart (1963), and χ is the correction factor that is used to generalize this model in describing the effect of void ratio. Figure 10 shows the dependency of axial component of plastic modulus on void ratio where

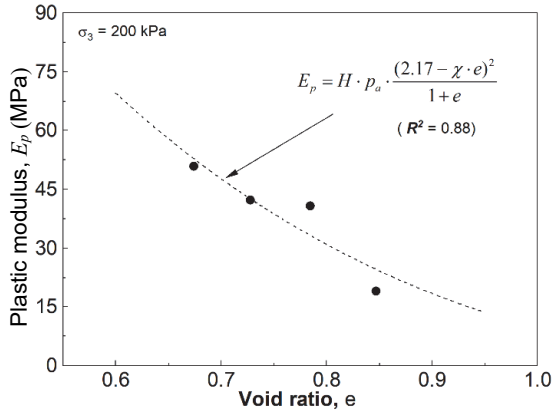

(a) CSTT

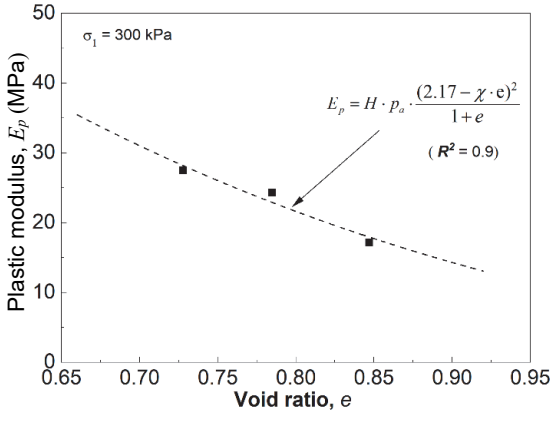

(b) CCCT

Fig. 10 Dependency of axial component of plastic modulus on the void ratio

the stress state is known due to loading condition. Combining the effects of loading cycle, stress state, and void ratio from Eqs. (3) ~ (6) brings the comprehensive form:

$$E_p = Q \cdot p_a \cdot \left(\psi - \phi \frac{\sigma_1}{p_a} \right) \cdot \left(\frac{\sigma_3}{p_a} \right)^m \cdot \frac{(2.17 - \chi \cdot e)^2}{1 + e} \cdot \exp(\eta \cdot N) \tag{7}$$

where Q is a newly introduced constant.

Note that Eqs. (4) ~ (6) were obtained empirically during the initial loading ($N = 1$). Since $\gamma_1(\sigma_1, \sigma_3, e)$ is a constant in Eq. (3), it can theoretically be derived and calibrated in each stress cycle. The influence of stress history on E_p was considered fully represented by N. By contrast, it was assumed that the dependence of the E_p on the stress state satisfied the same criterion under different stress conditions. The empirical Eq. (4) can be directly embedded in Eq. (5), which completely characterized the dependence of the E_p on the stress state. This dependency also requires further versification under more stress conditions to accurately present the evolutionary behavior of E_p of granular soils. Furthermore, E_p is decoupled from E and E_e, and because of that E_e is obtained in a deformation steady state, the parameters in Eq. (7) can only be calibrated in the pre-failure stage. As shown in Eq. (7), E_p decreases continuously during shearing; however, it did not decrease indefinitely until the lower threshold was met. It was boldly assumed that when the plastic modulus approached a threshold in shear, the specimen reached a critical state. Consequently, E_p in this paper only reflects the hardening behavior.

3.4 Total Strain Increment in Cyclic Loading

Even though the induced strain was small in each reloading process, the cumulative effect of a large number of loading cycles caused excessive deformation and showed significant effects on the integrity of the overlying infrastructure on cyclically loaded soil. Therefore, the prediction for cumulative deformations of sands under cyclic loading played an important role in engineering design. The strain accumulation depended on the strain increment in each cycle. The axial strain increment can be calculated by

$$\Delta\varepsilon = \frac{\Delta\sigma_1}{E_e} + \frac{\Delta\sigma_1}{E_p} \tag{8}$$

At specified stress increment $\Delta\sigma_1$ in each cycle, $\Delta\varepsilon$ as total strain increment can be measured directly. By Eq. (8), the calculated $\Delta\varepsilon$ and measured $\Delta\varepsilon$ can be compared to present the performance of E_e and E_p. To calculate $\Delta\varepsilon$ by Eq. (8), E_e and E_p need to be determined. The E_p was obtained in this study from Eq. (7). The E_e can be obtained using the deformation steady state. An empirical formulation for elastic modulus considering the effect of confining pressure and void ratio is adopted, which was proposed by a previous study (Shao *et al.* 2018), as follows:

$$E_e = P \cdot p_a \cdot \left(M + \alpha \cdot \frac{\sigma_1}{p_a} \right) \cdot \frac{(2.17 - \beta \cdot e)^2}{1 + e} \tag{9}$$

where P, M, α, and β are the constant parameters. These four elastic parameters were obtained at the deformation steady state. The axial strain increments versus cycles are shown in Fig. 11. The experimental results and prediction by Eq. (8) were compared and

showed reasonable agreement. The values of all the parameters for the silica sand are summarized in Table 3. This good agreement validated the accuracy of elastic and plastic moduli evolution. It provided an effective way to characterize total deformation in cyclic loading, rather than an assumption about plasticity theory.

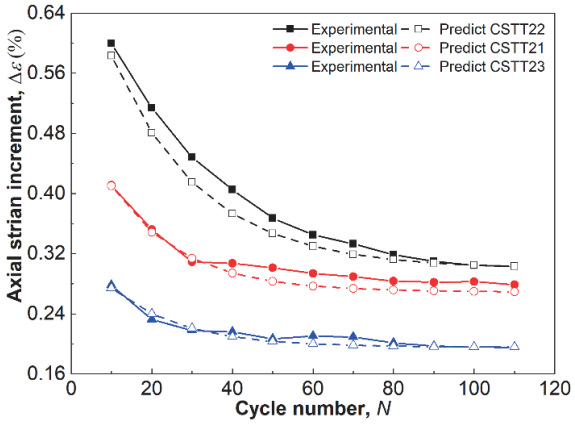

(a) CSTT

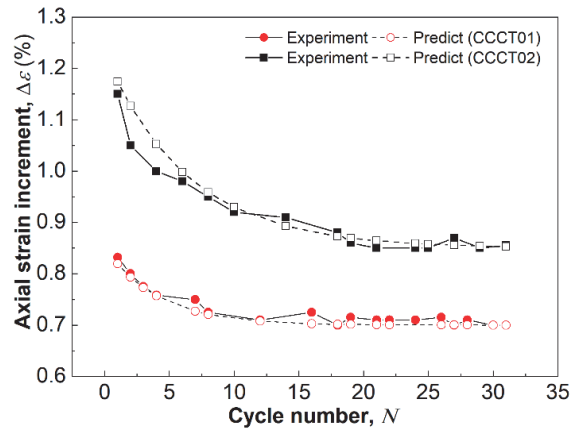

(b) CCCT

Fig. 11 Comparison of prediction of axial strain increment and experimental results

Table 3 Model parameters

Parameters / Test	P	M	α	β	Q	ψ	ϕ	m	χ	η
CSTT	0.537	23.5	821	0.43	1952	–	–	1.81	1.69	0.057
CCCT	0.836	0.5	328	0.884	20	87	1.685	0.58	1.34	0.202

4. DISCUSSION

4.1 Justification of Deformation Steady State

To facilitate the following discussion, two new strains were introduced: creep strain and residual strain. They both emerged per cycle under slow periodic load. Figure 12 shows the detailed evolution of different strain components. According to the load pattern in a single cycle, the given stress increment is applied to the specimen instantaneously, and then instantaneous strain is generated. Subsequently, the stress level is kept constant, resulting in creep strain (denoted as $\Delta\varepsilon_c$). The instantaneous strain includes elastic and plastic strain components (denoted as $\Delta\varepsilon_e + \Delta\varepsilon_p^{in}$). The subsequent creep strain is attributed to the plastic part due to its irreversible nature. Therefore, in a complete load cycle, the total strain increment is still elastic strain increment and plastic strain increment. Eq. (1) can be rewritten as:

$$\Delta\varepsilon_p = \Delta\varepsilon_p^{in} + \Delta\varepsilon_c \tag{10a}$$

$$\Delta\varepsilon = \Delta\varepsilon_e + \Delta\varepsilon_p^{in} + \Delta\varepsilon_c \tag{10b}$$

where $\Delta\varepsilon_p^{in}$ is the instantaneous plastic strain increment as an instantaneous response to stress increments. In terms of strain type, $\Delta\varepsilon_p^{in}$ and $\Delta\varepsilon_c$ are plastic strain increments, and $\Delta\varepsilon_e$ is an elastic strain increment; in terms of time effect, $\Delta\varepsilon_e$ and $\Delta\varepsilon_p^{in}$ are instantaneous strain increments, and $\Delta\varepsilon_c$ is a creep strain increment. In addition, residual strain (denoted as ε_{res}) is the accumulated strain at the end of stress unloading per cycle. Noted that the composition of plastic strain includes $\Delta\varepsilon_p^{in}$ and $\Delta\varepsilon_c$ in Eq. 10(a). When analyzing the time dependence of the stress-strain behavior of sand, it is better to treat them as an integral plastic (irreversible) strain. For more details, refer to Di Benedetto *et al.* (2002).

This section focused on the justification of deformation steady state by providing experimental evidence to support the previous assumption. The assumption stated that the elastic strain increment was constant during the slow periodic load and was obtained accurately from the deformation steady state. By the definition of deformation steady state, the specimen response does not change dramatically, and the stress-strain curve was a closed hysteretic loop when it was subjected to a certain cyclic loading. This deformation steady state was justified in this section by the concept of modulus growth rate. This method justified the same evolution form of deformation moduli and residual strain growth rate.

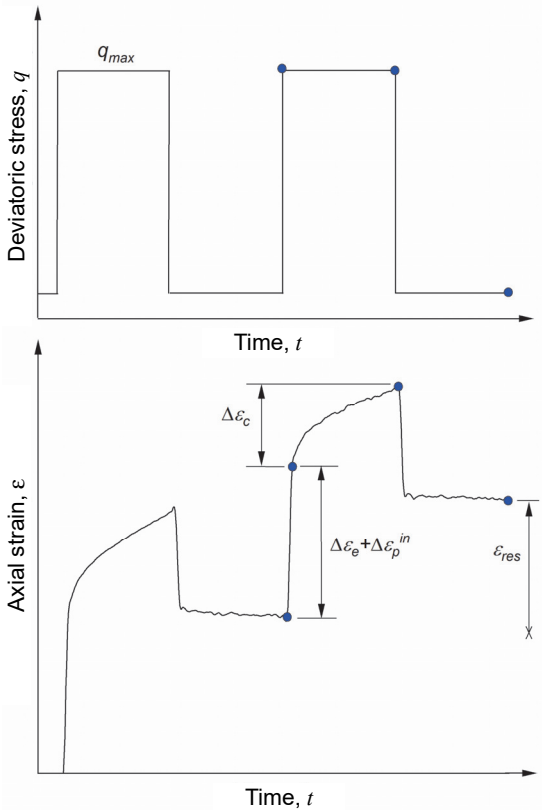

Fig. 12 Definitions of creep strain and residual strain (data from CSTT22)

Hence, the elastic strain growth rate becomes zero and elastic strain increment becomes constant, which is the pivotal concept for deformation steady state.

The deformation modulus gradually increased as the loading cycles rose. Deformation modulus growth rate R is defined to describe the evolution of deformation modulus. Its form can be derived from

$$R = \frac{E^{i+1} - E^{i}}{E^{i}} = \frac{\Delta\varepsilon^{i} - \Delta\varepsilon^{i+1}}{\Delta\varepsilon^{i+1}} = \frac{\Delta\varepsilon_e^{i+1}}{\Delta\varepsilon^{i+1}} \cdot \frac{\Delta\varepsilon_e^{i} - \Delta\varepsilon_e^{i+1}}{\Delta\varepsilon_e^{i+1}} + \frac{\Delta\varepsilon_p^{i+1}}{\Delta\varepsilon^{i+1}} \cdot \frac{\Delta\varepsilon_p^{i} - \Delta\varepsilon_p^{i+1}}{\Delta\varepsilon_p^{i+1}} = \lambda \cdot R_e + \kappa \cdot R_p \tag{11}$$

where superscript i denotes the i^{th} loading cycle; R_e is elastic strain growth rate, defined as $R_e = (\Delta\varepsilon_e^{i} - \Delta\varepsilon_e^{i+1}) / \Delta\varepsilon_e^{i+1}$; R_p is plastic strain growth rate, defined as $R_p = (\Delta\varepsilon_p^{i} - \Delta\varepsilon_p^{i+1}) / \Delta\varepsilon_p^{i+1}$; λ is elastic coefficient, defined as $\lambda = \Delta\varepsilon_e^{i+1} / \Delta\varepsilon^{i+1}$ in the range $0 < \lambda \le 1$; κ is plastic coefficient, defined as $\kappa = \Delta\varepsilon_p^{i+1} / \Delta\varepsilon^{i+1}$ in the range $0 \le \kappa < 1$. Equation (11) is obtained from the combination of Eq. (2d) and those parameters definitions. It shows that the evolution of deformation modulus can be expressed as a linear interpolation of the evolution of elastic and plastic strains.

Similarly, corresponding to residual strain ε_{res}, the residual strain growth rate R_{res} is defined as $R_{res} = (\Delta\varepsilon_{res}^{i} - \Delta\varepsilon_{res}^{i+1}) / \Delta\varepsilon_{res}^{i+1}$. R_{res} and R_p are intrinsically related. Specifically, the evolution of plastic strain with cycles caused the accumulation of residual strain. In this regard, the evolution of plastic strain was inherently linked to the evolution of residual strain. This statement was further confirmed by the creep strain (see Fig. 13(a)). Creep strain presents a similar behavior with plastic strain based on the fact that creep and plastic strains have similar plastic potential (Desai and Zhang 1987; Lade and Liu 1998; Wang *et al.* 2011). In this way, the variation of the plastic strain increment with cycles was presented by the evolution of the residual strain. This relation was confirmed by data in Fig. 13(b) where the exponential form for residual strain remained the same as Eq. (3) for the axial component of plastic modulus. Therefore, the relation between R_p and R_{res} is justified and can be expressed as

$$R_p = \omega \cdot R_{res} \tag{12}$$

where ω is the coefficient in the relation.

Substituting Eq. (12) into Eq. (11) gives

$$R = \lambda \cdot R_e + \kappa \cdot \omega \cdot R_{res} \tag{13}$$

Variation of R and R_{res}, with respect to N in both CSTT and CCCT, is shown in Fig. 14, indicating that R and R_{res} followed the same evolution form within the fitting tolerance. In Eq. (13), to ensure that R and R_{res} remain in the same functional form, the coefficient $\kappa \cdot \omega$ is set as 1. Then, $\lambda \cdot R_e = 0$ holds, which means that elastic strain growth rate is zero. It can be expressed as

$$\Delta\varepsilon_e^{i} = \Delta\varepsilon_e^{i+1} \tag{14}$$

Equation (14) reveals that the elastic strain increment was constant and independent of the axial cyclic loading, which provided some evidence for the previous assumption.

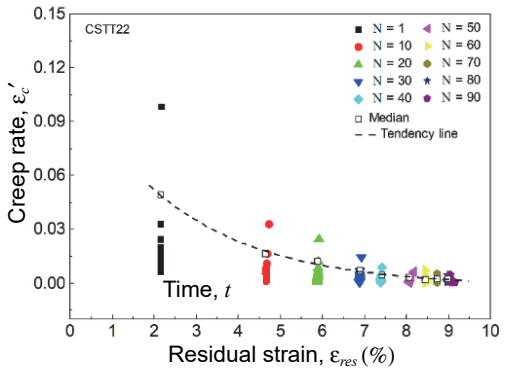

(a)

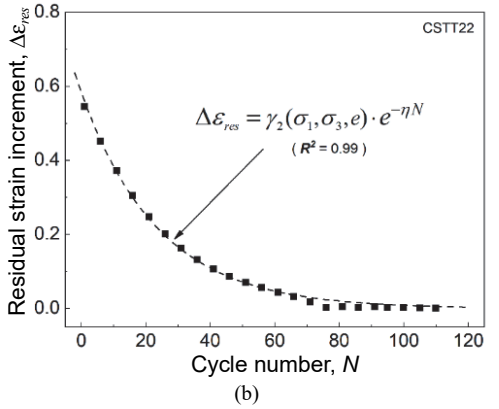

(b)

Fig. 13 (a) Relation between creep strain rate and residual strain and (b) evolution of residual strain increment with number of cycles

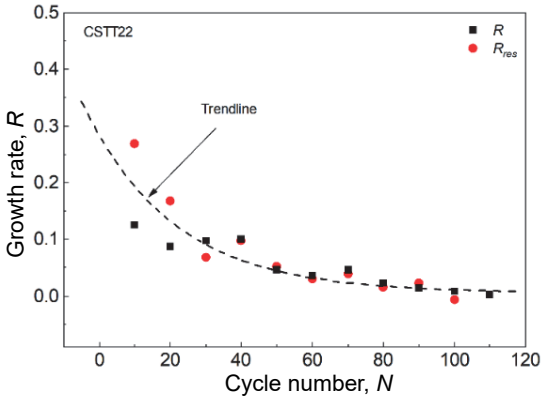

(a) CSTT

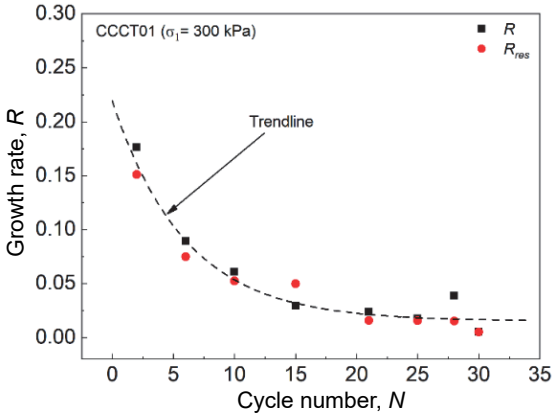

(b) CCCT

Fig. 14 Change of growth rate with number of cycles

4.2 Unloading Strain in Periodic Loading

Previous deformation analysis was concerned with reloading processes in cyclic loading. In addition to the deformation in the reloading process, the deformation in the unloading process was also of practical importance; for example, volume contraction. Volume contraction during the unloading process is one of the fundamental properties of granular materials that cannot be explained and described by conventional elastic and plastic theories (Li and Guo 2000; Chi *et al.* 2009; Chi *et al.* 2010). Li and Guo (2000) attributed volume contraction to the partial reverse of dilatancy. The dilatancy of soil is caused by the relative movement between the interlocking particles, and it is treated as an irreversible process (Pradhan *et al.* 1989 and Wahyudi *et al.* 2010). However, in unloading with certain confining pressure, partial dilatancy can be recovered and volume contraction is the consequence of this partial dilatancy. Thus, this section explained the mechanism of volume contraction in the unloading process by virtue of unloading strain. For more description of the stress-dilatancy relation under cyclic loading refer to Pradhan *et al.* (1989), Pradhan and Tatsuoka (1989), and Wahyudi *et al.* (2010).

Figure 15(a) is a total cumulative axial strain evolution curve. In the process of cyclic hardening, the strain increment produced by each stress cycle gradually decreased. The involved strain in the unloading process is plotted in Fig. 15(a). The oscillating grey curve is the reloading-unloading curve. The blue curve is the connection of the local peak points on the grey curve, denoting the evolution of reloading strain. The green curve is the connection of local trough points on the grey curve, denoting the evolution of residual strain. In each loading cycle, the elastic strain was calculated, and it formed the dim grey zone. The difference between the reloading total strain and the elastic strain is the reloading plastic strain, which is marked as the black dash curve. The difference between reloading plastic strain and residual strain is the unloading plastic strain, which is indicated by a bright grey zone. This zone represents the reversible part of dilatancy. In Fig. 15(a), the unloading process is indicated by the space from blue curve to green curve, which has an elastic strain component and an unloading plastic component. The elastic strain emerged during the reloading process and was fully released during the unloading process. Whereas, the unloading plastic strain emerged during the unloading process and was related to the movement of sand particles. Thus, the occurrence of unloading plastic strain was not explained by classical plastic theory. In addition, the unloading plastic strain was the principal component of the volume contraction in unloading. Figure 15(a) shows that volumetric contraction (partially represented by bright grey zone) in the unloading process depended on stress history. This dependence became weaker and eventually almost vanished with more loading cycles. This phenomenon was explained by the microstructure change of the specimen (Li and Guo 2000; Zhao and Zhang 2014). Figure 15(b) is a schematic diagram corresponding to particle movement. In the reloading process, the relative motion between granules, such as sliding, rolling and climbing, resulted in volumetric dilatancy at certain cyclic loading. In this circumstance, some particles became unstable. When going into the unloading process, these particles returned to their original positions, which caused a volumetric contraction in unloading, as schematically shown in Fig. 15(b) (the volume unit changed from the dotted line to the solid line position). As the loading cycles proceeded, more particles reached a stable state, which caused a reduction in relative movement between adjacent particles. Furthermore, observation of the microscopic motion between particles and exploration of the microscopic mechanism of dilatancy by DEM is recommended for extended future research.

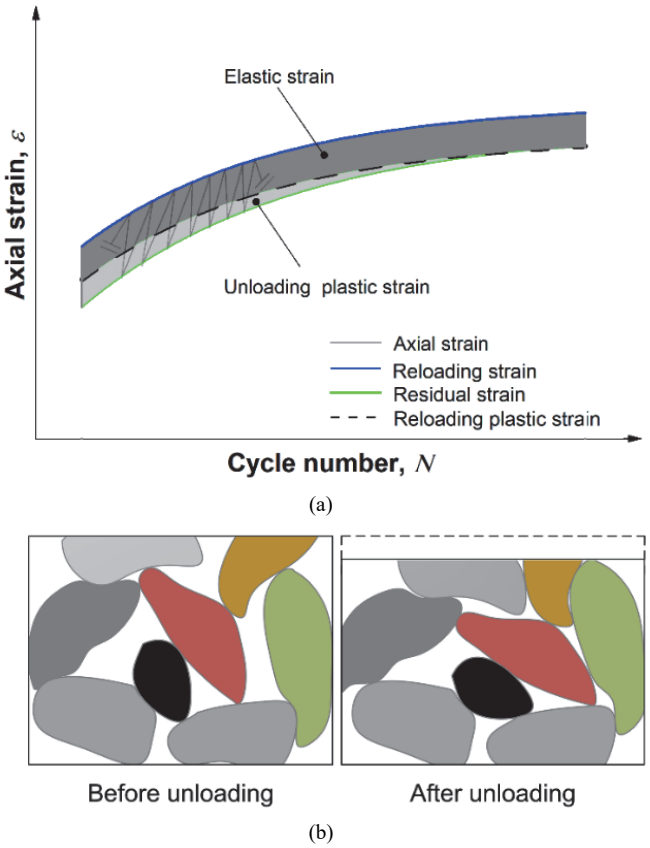

Fig. 15 Deformation response in unloading: (a) evolution of unloading strain with the number of cycles (data from CSTT22) and (b) sketch to highlight microstructure change of specimen by unloading

5. CONCLUSIONS

In this study, a static triaxial compression system was designed to perform a series of slow periodic loads on silica sand. The newly designed static test system provided long-period constant load and embedded optical measurement methods to measure the overall axial and radial strains of the specimen without disturbance. The specimens were subjected to stress cycles under triaxial stress and confined stress conditions. In the initial loading cycles, the deformation modulus mainly depended on the axial component of plastic modulus, and it began to weigh on the elastic modulus after certain cyclic loading cycles. The axial component of plastic modulus increased with increased confining pressure or decreased initial void ratio; however, it decreased linearly with increased axial stress, consequently, an empirical model for the axial component of the plastic modulus in cyclic loading was proposed considering the effects of axial stress, confining pressure, initial void ratio, and the number of cycles. This paper presented the evolution of the moduli for sand with the concept of decoupling, in particular, to better understand the evolution of the axial component for plastic modulus. Furthermore, observing the microscopic motion between particles and exploring the microscopic mechanism of dilatancy by DEM is recommended for extended research.

FUNDING

This work is supported by the National Natural Science Foundation of China (No. 52079018), and National Key Laboratory Funding of Independent Research Project (No. S18406).

DATA AVAILABILITY

The data and/or computer codes used/generated in this study are available from the corresponding author on reasonable request.

CONFLICT OF INTEREST STATEMENT

The authors declare that there is no conflict of interest.

REFERENCES

Anhdan, L. and Koseki, J. (2004). "Effects of large number of cyclic loading on deformation characteristics of dense granular materials." *Soils and Foundations*, **44**(3), 115-123. https://doi.org/10.3208/sandf.44.3_115

Cen, W.J., Luo, J.R., Bauer, E., and Zhang, W.D. (2018). "Generalized plasticity model for sand with enhanced state parameters." *Journal of Engineering Mechanics*, ASCE, **144**(12), 04018108. https://doi.org/10.1061/(ASCE)EM.1943-7889.0001534

Chi, M.J., Zhao, C.G., and Li, X.J. (2009). "Stress-dilation mechanism of sands." *China Civil Engineering Journal*, **42**(3), 99-104. https://doi.org/10.15951/j.tmgcxb.2009.03.013

Chi, M.J., Li, X.J., Zhao, C.G., Zhou, Z.H., and Zhao, J.S. (2010). "Meso-scale study on volume-contraction of sand during unloading process." *Journal of Basic Science and Engineering*, **18**, 181-188. https://doi.org/10.3969/j.issn.1005-0930.2010.s1.021

Chiou, J.S., Lin, H.S., Yeh, F.Y., and Sung, Y.C. (2016). "Plastic settlement evaluation of embedded railroads under repeated train loading." *Journal of GeoEngineering*, TGS, **11**(2)**,** 97-107. http://dx.doi.org/10.6310/jog.2016.11(2).5

Dafalias, Y.F. and Herrmann, L.R. (1986). "Bounding surface plasticity. II: Application to isotropic cohesive soils." *Journal of Engineering Mechanics*, ASCE, **112**(12), 1263-1291. https://doi.org/10.1061/(ASCE)0733-9399(1986)112:12(1263)

Dafalias, Y.F. and Manzari, M.T. (2004). "Simple plasticity sand model accounting for fabric change effects." *Journal of Engineering Mechanics*, ASCE, **130**(6), 622-634. https://doi.org/10.1061/(ASCE)0733-9399(2004)130:6(622)

Dafalias, Y.F. and Popov, E.P. (1975). "A model of nonlinearly hardening materials for complex loading." *Acta Mechanica*, **21**(1), 173-192. https://doi.org/10.1007/BF01181053

Dareeju, B., Gallage, C., Ishikawa, T., Dhanasekar, M., and Dawes, L. (2018). "Effects of particle size distributions and principal stress axis rotation on cyclic plastic deformation characteristics of coarse materials." *Journal of GeoEngineering*, TGS, **13**(4), 161-170. http://dx.doi.org/10.6310/jog.201812_13(4).1

Das, S. (2014). *Three Dimensional Formulation for the Stress-Strain-Dilatancy Elasto-Plastic Constitutive Model for Sand under Cyclic Behaviour.* Ph.D. Dissertation, University of Canterbury, Christchurch, New Zealand.

Desai, C.S. and Zhang, D. (1987). "Viscoelastic model for geological material with generalized flow rule." *International Journal for Numerical and Analytical Methods in Geomechanics*, **11**(6), 603-620. https://doi.org/10.1002/nag.1610110606

Di Benedetto, H., Tatsuoka, F., and Ishihara, M. (2002). "Time-dependent shear deformation characteristics of sand and their constitutive modelling." *Soils and Foundations*, **42**(2), 1-22. https://doi.org/10.3208/sandf.42.2_1

Hardin, B.O. (1978). "The nature of stress-strain behavior for soils." *Proceedings of the ASCE Geotechnical Engineering Division Specialty Conference*, June 19-21, Pasadena, California, U.S.A.

Hardin, B.O. and Blandford, G.E. (1989). "Elasticity of particulate materials." *Journal of Geotechnical Engineering*, ASCE, **115**(6), 788-805. https://doi.org/10.1061/(ASCE)0733-9410(1989)115:6(788)

Hardin, B.O. and Drnevich, V.P. (1972). "Shear modulus and damping in soils, measurement and parameter effects." *Journal of the Soil Mechanics and Foundations Division*, ASCE, **98**(6), 603-624.

Hardin, B.O. and Richart, F.E. (1963). "Elastic wave velocities in granular soils." *Journal of the Soil Mechanics and Foundations Division*, ASCE, **89**(sm1), 33-66.

Hashiguchi, K. (1989). "Subloading surface model in unconventional plasticity." *International Journal of Solids and Structures*, **25**(8), 917-945. https://doi.org/10.1016/0020-7683(89)90038-3

Heidarzadeh, H. and Oliaei, M. (2018a). "Development of a generalized model using a new plastic modulus based on bounding surface plasticity." *Acta Geotechnica*, **13**(4), 925-941. https://doi.org/10.1007/s11440-017-0599-0

Heidarzadeh, H. and Oliaei, M. (2018b). "An efficient generalized plasticity constitutive model with minimal complexity and required parameters." *KSCE Journal of Civil Engineering*, **22**(4), 1109-1120. https://doi.org/10.1007/s12205-017-1037-4

Hicher, P. (1996). "Elastic properties of soils." *Journal of Geotechnical Engineering*, ASCE, **122**(8), 641-648. https://doi.org/10.1061/(ASCE)0733-9410(1996)122:8(641)

Hongnam, N. and Koseki, J. (2019). "Modeling quasi-elastic properties of sand while considering inherent and stress-induced anisotropies." *KSCE Journal of Civil Engineering*, **23**(5), 1990-1998. https://doi.org/10.1007/s12205-019-0694-x

Hoque, E. and Tatsuoka, F. (1998). "Anisotropy in elastic deformation of granular materials." *Soils and Foundations*, **38**(1), 163-179. https://doi.org/10.3208/sandf.38.163

Hoque, E. and Tatsuoka, F. (2004). "Effects of stress ratio on small-strain stiffness during triaxial shearing." *Geotechnique*, **54**(7), 429-439. https://doi.org/10.1680/geot.2004.54.7.429

Iwan, W.D. (1967). "On a class of models for the yielding behavior of continuous and composite systems." *Journal of Applied Mechanics*, **34**(3), 612-617. https://doi.org/10.1115/1.3607751

Karg, C. and Haegeman, W. (2009). "Elasto-plastic long-term behavior of granular soils: Experimental investigation." *Soil Dynamics and Earthquake Engineering*, **29**(1), 155-172. https://doi.org/10.1016/j.soildyn.2008.01.001

Kohata, Y., Tatsuoka, F., Wang, L., Jiang, G.L., Hoque, E., and Kodaka, T. (1997). "Modelling the non-linear deformation properties of stiff geomaterials." *Géotechnique*, **47**(3), 563-580. https://doi.org/10.1680/geot.1997.47.3.563

Kongsukprasert, L. and Tatsuoka, F. (2007). "Small strain stiffness and non-linear stress-strain behaviour of cement-mixed

gravelly soil." *Soils and Foundations*, **47**(2), 375-394. https://doi.org/10.3208/sandf.47.375

Lade, P.V. and Liu, C.T. (1998). "Experimental study of drained creep behavior of sand." *Journal of Engineering Mechanics,* ASCE, **124**(8), 912-920. https://doi.org/10.1061/(ASCE)0733-9399(1998)124:8(912)

Li, G.X. and Guo, R.P. (2000). "Volume-contraction in unloading of shear tests and reversible dilatation of soils." *Chinese Jounal of Geotechnical Engineering*, **22**(2), 158-161.

Ling, H.I. and Liu, H. (2003). "Pressure-level dependency and densification behavior of sand through generalized plasticity model." *Journal of Engineering Mechanics*, ASCE, **129**(8), 851-860. https://doi.org/10.1061/(ASCE)0733-9399(2003)129:8(851)

Ling, H.I. and Yang, S. (2006). "Unified sand model based on the critical state and generalized plasticity." *Journal of Engineering Mechanics*, ASCE, **132**(12), 1380-1391. https://doi.org/10.1061/(ASCE)0733-9399(2006)132:12(1380)

Liu, X. (2012). *Method of Entire Surface Deformation Measurement for Soil Specimen in Triaxial Tests and Its Application*. Ph.D. Dissertation, Dalian University of Technology, Dalian, China.

Mróz, Z. (1967). "On the description of anisotropic hardening." *Journal of the Mechanics and Physics of Solids*, **15**(3), 163-175. https://doi.org/10.1016/0022-5096(67)90030-0

Mroz, Z., Norris, V.A., and Zienkiewicz, O.C. (1979). "Application of an anisotropic hardening model in the analysis of elasto–plastic deformation of soils." *Géotechnique*, **29**(1), 1-34. https://doi.org/10.1680/geot.1979.29.1.1

Pradhan, T.B.S., Tatsuoka, F., and Sato, Y. (1989). "Experimental stress-dilatancy relations of sand subjected to cyclic loading." *Soils and Foundations*, **29**(1), 45-64. https://doi.org/10.3208/sandf1972.29.45

Pradhan T.B.S. and Tatsuoka F. (1989). "On stress-dilatancy equations of sand subjected to cyclic loading." *Soils and Foundations*, **29**(1), 65-81. https://doi.org/10.3208/sandf1972.29.65

Sawicki, A. and Świdziński, W. (1998). "Elastic moduli of noncohesive particulate materials." *Powder Technology*, **96**(1), 24-32. https://doi.org/10.1016/S0032-5910(97)03354-8

Shao, L.T., Liu, G., Zeng, F.T., and Guo, X.X. (2016). "Recognition of the stress-strain curve based on the local deformation measurement of soil specimens in the triaxial test." *Geotechnical Testing Journal*, **39**(4), 658-672. https://doi.org/10.1520/GTJ20140273

Shao, L.T., Liu, X., Guo, X.X., Huang, C., Ju, P., Yang, S., and Xue, J. (2012). "Whole surface deformation measurement of triaxial soil specimen based on digital image processing." *Chinese Journal of Geotechnical Engineering*, **34**(3), 409-415. https://doi.org/CNKI:SUN:YTGC.0.2012-03-008

Shao, L.T., Xia, P.X., Zeng, F.T., and Guo, X.X. (2018). "Investigation on the tangent Young's modulus of sands in reloading of cyclic triaxial tests." *Electronic Journal of Geotechnical Engineering*, **23**(5), 607-623.

Shibuya, S., Tatsuoka, F., Teachavorasinskun, S., Kong, X., Abe, F., Kim, Y., and Park, C. (1992). "Elastic deformation properties of geomaterials." *Soils and Foundations*, **32**(3), 26-46. https://doi.org/10.3208/sandf1972.32.3_26

Shin, E.C. and Das, B.M. (1999). "Dynamic behavior of geogrid-reinforced sand." *KSCE Journal of Civil Engineering*, **3**(4), 379-386. https://doi.org/10.1007/BF02830473

Taheri, A. and Tatsuoka, F. (2012). "Stress–strain relations of cement-mixed gravelly soil from multiple-step triaxial compression test results." *Soils and Foundations*, **52**(4), 748-766. https://doi.org/10.1016/j.sandf.2012.07.014

Taheri, A. and Tatsuoka, F. (2015). "Small- and large-strain behaviour of a cement-treated soil during various loading histories and testing conditions." *Acta Geotechnica*, **10**(1), 131-155. https://doi.org/10.1007/s11440-014-0339-7

Tatsuoka, F. and Kohata, Y. (1995). "Stiffness of hard soils and soft rocks in engineering applications." *Pre-failure Deformation Characteristies of Geomaterials: Proceedings of the International Symposium*, September 12-14, Sapporo, Japan.

Wahyudi S., Chiaro, G., De Silva L.I.N., and Koseki, J. (2010). "Stress-dilatancy behavior of loose sand during drained cyclic torsional shear loading." *12th International Summer Symposium of JSCE*, September 18, Chiba, Japan.

Wang, Z.C., Qiao, L.P., Li, S.C., and Lin, C.J. (2011). "An internal-variable creep model for soils." *Chinese Journal of Geotechnical Engineering*, **33**(10), 1565-1575. https://doi.org/10.1111/j.1759-6831.2010.00113.x

Weng, M.C. (2013). "A generalized plasticity-based model for sandstone considering time-dependent behavior and wetting deterioration." *Rock Mechanics and Rock Engineering*, **47**(4), 1197-1209. https://doi.org/10.1007/s00603-013-0466-8

Wichtmann, T., Niemunis, A., and Triantafyllidis, T. (2005). "Strain accumulation in sand due to cyclic loading: Drained triaxial tests." *Soil Dynamics and Earthquake Engineering*, **25**(12), 967-979. https://doi.org/10.1016/j.soildyn.2005.02.022

Zeng, F.T. and Shao, L.T. (2016). "Unloading elastic behavior of sand in cyclic triaxial tests." *Geotechnical Testing Journal*, **39**(3), 1-14. https://doi.org/10.1520/GTJ20150171

Zhao, C.L. and Zhang, W.H. (2014). "Plastic modulus of saturated dense sands under cyclic loading." *Construction and Maintenance of Railway Infrastructure in Complex Environment*, **1**, 342-345.

Zhao, Z.Y., Deng, G., Han, Y.S., Zhang, Z.P., Dong, Y.L., and Gao, Y. (2020). "Comparison of deformation behavior of saturated sand under constant and variable deviatoric stress." *KSCE Journal of Civil Engineering*, **24**(3), 762-769. https://doi.org/10.1007/s12205-020-0976-3

Zienkiewicz, O.C. and Mroz, Z. (1984). "Generalized plasticity formulation and applications to geomechanics." In: Desai, C.S. and Gallagher, R.H., Eds., *Mechanics of Engineering Materials*. John Wiley, New York, U.S.A., 655-680.